Journal of Computational Physics 228 (2009) 5323–5339

Contents lists available at ScienceDirect

Journal of Computational Physics

journal homepage: www.elsevier.com/locate/jcp

Stable and efficient finite-difference nonlinear-multigrid schemes for the phase field crystal equation

Z. Hu [a], S.M. Wise [b], C. Wang [c], J.S. Lowengrub [a,*]

[a] Department of Mathematics, The University of California, Irvine, CA 92697-3875, USA
[b] Department of Mathematics, The University of Tennessee, Knoxville, TN 37996-1300, USA
[c] Department of Mathematics, The University of Massachusetts, North Dartmouth, MA 02747-2300, USA

ARTICLE INFO

Article history:
Received 6 October 2008
Received in revised form 8 April 2009
Accepted 9 April 2009
Available online 23 April 2009

Keywords:
Phase field crystal
Finite difference
Energy stability
Multigrid

ABSTRACT

In this paper we present and compare two unconditionally energy stable finite-difference schemes for the phase field crystal equation. The first is a one-step scheme based on a convex splitting of a discrete energy by Wise et al. [S.M. Wise, C. Wang, J.S. Lowengrub, An energy stable and convergent finite-difference scheme for the phase field crystal equation, SIAM J. Numer. Anal., in press]. In this scheme, which is first order in time and second order in space, the discrete energy is non-increasing for any time step. The second scheme we consider is a new, fully second-order two-step algorithm. In the new scheme, the discrete energy is bounded by its initial value for any time step. In both methods, the equations at the implicit time level are nonlinear but represent the gradients of strictly convex functions and are thus uniquely solvable, regardless of time step-size. We solve the nonlinear equations using an efficient nonlinear multigrid method. Numerical simulations are presented and confirm the stability, efficiency and accuracy of the schemes.

1. Introduction

Most crystals have defects, such as vacancies, grain boundaries, and dislocations. Such imperfections control, to a large extent, the macroscopic properties of crystalline materials, and an understanding of their formation and evolution is of great interest. Defects pose a considerable challenge to modeling and numerical simulation because of the complexity they introduce. One model that has shown great versatility in simulating defects is the phase field crystal (PFC) equation proposed by Elder et al. [3,4] to study the dynamics of atomic-scale crystal growth on diffusive time scales. In the PFC model, a phase-field formulation is introduced that accounts for the periodic structure of a crystal lattice through a free energy functional of Swift–Hohenberg type [14] that is minimized by periodic functions. The model naturally incorporates elastic and plastic deformation of the crystal and the various crystal defects. The idea of the PFC is that a conserved phase variable is introduced to describe a coarse-grained temporal average of the number density of atoms. Consequently, this method represents a significant advantage over other atomistic methods such as molecular dynamics where the time steps are constrained by atomic-vibration time scales. The PFC approach is related to dynamic density functional theory [10,1]. The recent review by Provatas et al. [13] details the many applications of the PFC equation.

The PFC equation is a high-order (sixth-order) nonlinear partial differential equation. Except for very special cases, the PFC equation cannot be solved analytically. Therefore, efficient numerical algorithms are essential. Previously, Elder et al. [3,4] solved the PFC equation using an explicit Euler scheme, where a high-order time step restriction ($s < Ch^6$) is required

* Corresponding author. Tel.: +1 949 824 2655; fax: +1 949 824 7993.
E-mail addresses: zhu@math.uci.edu (Z. Hu), swise@math.utk.edu (S.M. Wise), cwang1@umassd.edu (C. Wang), lowengrb@math.uci.edu (J.S. Lowengrub).

0021-9991/$ - see front matter © 2009 Elsevier Inc. All rights reserved.
doi:10.1016/j.jcp.2009.04.020

for stability. More recently, Mellenthin et al. [11] proposed a pseudo-spectral scheme in which an integrating factor method, based on the linear terms, is used in Fourier space. Because a backward diffusive term is incorporated in the integrating factor, this term may significantly amplify low-to-moderate wavenumbers at large time steps and introduce accuracy-related (and possibly stability-related) time step restrictions. In general, spectral methods have the potential to be more accurate than lower order finite-difference methods. Further, the use of fast, parallel Fourier transforms enables these schemes to potentially be highly efficient. However, the results may sensitive to discretization parameters since this approach combines spatial and temporal errors. For example, seemingly equilibrated interfaces may actually be associated with an oscillatory chemical potential and equilibria may sensitively depend on the time step. (See Leo et al. [9] for more details.) In addition, unlike the finite difference method, the spectral method requires periodic boundary conditions and spatially uniform meshes. In [2], Cheng and Warren introduced a linearized splitting scheme, similar to that analyzed in [16]. Cheng and Warren's scheme depends on standard Fourier stability analysis of a linearized PFC equation, where the nonlinear term ϕ^3 (see Eq. (3)) in the chemical potential is treated explicitly. A semi-implicit finite element method was introduced by Backofen et al. [1]. Their method is essentially a standard backward Euler scheme, but where the nonlinear term ϕ^3 in the chemical potential is linearized via $(\phi^{k+1})^3 \approx 3(\phi^k)^2\phi^{k+1} - 2(\phi^k)^3$. No stability analysis is given, though they claim that relatively large step sizes can be achieved. None of the preceding works propose energy stable methods, *i.e.*, methods for which the energy is bounded by its value at the previous time step (strong energy stability) or by its initial value (weak energy stability). The schemes described above are all linear, and thus conditions on solvability are somewhat more accessible. We point out that because Backofen et al. discretize a backwards diffusive term implicitly (specifically, the $2\Delta\phi$ term in Eq. (3)) their scheme is not expected to be unconditionally uniquely solvable.

In this paper, we present and compare two unconditionally energy stable finite-difference schemes for the PFC equation. The first is a one-step scheme based on a convex splitting of a discrete energy and is first order in time and second order in space. This method was proposed and analyzed in [19], but no numerical results were presented in that work. The second is a new two-step scheme and is fully second order. In both cases the equations at the implicit time level are nonlinear but represent the gradients of strictly convex functions and are thus uniquely solvable, regardless of time step-size. Although we focus on two-dimensions here, our analysis and numerical schemes apply equally well in three-dimensions. Herein we use periodic boundary conditions for simplicity. However, this is not a constraint, as our analysis of the schemes works for homogeneous Neumann and mixed period-homogeneous Neumann boundary conditions as well. In fact, in our last simulation (Figs. 7a–7d) we use the latter conditions. To efficiently solve the discrete systems at the implicit time-level, we use a nonlinear full approximation storage (FAS) multigrid method [15]. The algorithm we use follows that developed for Cahn–Hilliard equations by Kim et al. [8] for uniform grids and extended by Wise et al. [18] to adaptive, block-structured Cartesian meshes. We demonstrate the convergence of both schemes numerically and the benefits of enhanced accuracy from the second-order scheme. We use the second-order scheme to simulate the growth of a polycrystal and the development of grain boundaries.

The contents of this paper are as follows. In Section 2, we introduce the phase field crystal (PFC) equation, and the closely-related Swift–Hohenberg (SH) equation. Therein we give a brief description of the fully discrete schemes that will be examined later in detail. In Section 3, we build up the machinery required to rigorously define and analyze the schemes. In Section 4, we present the schemes in detail and demonstrate their properties, including the unique solvability and discrete-energy stability of our schemes. In Section 5, we briefly describe the nonlinear multigrid methods used to solve the nonlinear equation at the implicit time level. In Section 6, numerical results are presented. We give some concluding remarks and suggest some future work in Section 7.

2. Phase field crystal equations and proposed numerical schemes

Herein we consider a dimensionless energy of the form [4,14]

$$E(\phi) = \int_\Omega \left\{ \frac{1}{4}\phi^4 + \frac{1-\epsilon}{2}\phi^2 - |\nabla\phi|^2 + \frac{1}{2}(\Delta\phi)^2 \right\} d\mathbf{x}, \tag{1}$$

where $\phi : \Omega \subset \mathbf{R}^2 \to \mathbf{R}$ is the density field, ϵ is a constant assumed to be less than 1, and ∇ and Δ are the gradient and Laplacian operators, respectively. Suppose that $\Omega = (0, L_x) \times (0, L_y)$. There are two common types of gradient dynamics on Ω: (i) non-conserved dynamics,

$$\partial_t \phi = -M(\phi)\mu, \tag{2}$$

where $M(\phi) > 0$ is a mobility, μ is the chemical potential defined as

$$\mu := \delta_\phi E = \phi^3 + (1-\epsilon)\phi + 2\Delta\phi + \Delta^2\phi \tag{3}$$

and $\delta_\phi E$ denotes the variational derivative with respect to ϕ; and *(ii)* conserved dynamics,

$$\partial_t \phi = \nabla \cdot (M(\phi)\nabla\mu). \tag{4}$$

For both dynamical equations ϕ and $\Delta\phi$ are assumed periodic on Ω; for the conserved dynamics equation μ is additionally taken to be periodic. We point out that the theory and numerical algorithms to follow apply for homogeneous Neumann

boundary conditions as well. Because the dynamical equations are of gradient type, it is easy to see that the energy (1) is non-increasing in time along the solution trajectories of either Eq. (2) or Eq. (4). Eq. (4) is a mass conservation equation where the flux is proportional to the gradient of the chemical potential. This, along with the periodic boundary conditions, ensures that $\int_\Omega \partial_t \phi \, d\mathbf{x} = 0$.

Eq. (2) is the Swift–Hohenberg (SH) equation [14] and is of fourth order in space. Eq. (4) is the phase field crystal (PFC) equation and is a sixth-order equation. This paper shall be primarily concerned with the PFC equation, though most of the theoretical results and numerical algorithms can be applied to the SH equation as well.

If $M = 1$ the proposed schemes for the PFC Eq. (4) can be described easily. The schemes with more general mobilities are given in Section 4. The convex-splitting scheme from [19], which is first order in time and second order in space, is

$$\phi^{k+1} - \phi^k = s\Delta_h \mu^{k+1}, \tag{5}$$

$$\mu^{k+1} := (\phi^{k+1})^3 + (1-\epsilon)\phi^{k+1} + 2\Delta_h \phi^k + \Delta_h \kappa^{k+1}, \tag{6}$$

$$\kappa^{k+1} := \Delta_h \phi^{k+1}, \tag{7}$$

where Δ_h represents the five-point stencil approximation of Laplacian operator. In [19], the convergence of this discrete scheme was established. No numerical results were presented however. The new, second-order scheme is

$$\phi^{k+1} - \phi^k = s\Delta_h \mu^{k+1/2}, \tag{8}$$

$$\mu^{k+1/2} := \frac{1}{4}(\phi^{k+1} + \phi^k)((\phi^{k+1})^2 + (\phi^k)^2) + \frac{1-\epsilon}{2}(\phi^{k+1} + \phi^k) + 3\Delta_h \phi^k - \Delta_h \phi^{k-1} + \Delta_h \kappa^{k+1/2}, \tag{9}$$

$$\kappa^{k+1/2} := \frac{1}{2}(\Delta_h \phi^{k+1} + \Delta_h \phi^k), \tag{10}$$

where $\phi^{-1} := \phi^0$. Note that the local truncation error for the initial step is second order which implies that the overall method is globally second order accurate. Evidence confirming this is presented in Section 6.

We mention that an alternate approach to the nonlinear convex splitting scheme (5)–(7) proposed here is a linear splitting scheme, as was suggested by Eyre [5] and He et al. [6] for the Cahn–Hilliard equation and by Xu and Tang [20] for a bistable epitaxial thin film equation. This would involve a splitting of the chemical potential such as

$$\mu^{k+1} = A(\phi^{k+1} - \phi^k) - B\Delta_h(\phi^{k+1} - \phi^k) + \Delta_h^2 \phi^{k+1} + (\phi^k)^3 + (1-\epsilon)\phi^k + 2\Delta_h \phi^k,$$

where the splitting parameters $A, B \geqslant 0$ must be determined in order to ensure stability. Unconditional unique solvability is guaranteed, thanks to the linearity and positivity of the respective terms. It is expected that, as in [20], the energy will be non-increasing in time provided A and B are sufficiently large, but that such A and B will depend on the unknown ϕ^{k+1} [20, inequality (2.14)]. The linear splitting method is extendable to higher-order schemes [6,20].

3. Discretization of two-dimensional space

Our primary goal in this section is to define some finite-difference operators and summation-by-parts formulae in two space dimensions that are used to derive and analyze the numerical schemes. As mentioned before, the theory and algorithms extend straightforwardly to three-dimensions.

3.1. Two-dimensional difference operators and summation-by-parts formulae

Here we use the notation and results for cell-centered functions from [19]. The reader is directed there for complete details. We begin with definitions of grid functions and difference operators needed for our discretization of two-dimensional space. Let $\Omega = (0, L_x) \times (0, L_y)$, with $L_x = m \cdot h$ and $L_y = n \cdot h$, where m and n are positive integers and $h > 0$ is the spatial step size. Consider the following three sets $E_m := \{i \cdot h \mid i = 0, \ldots, m\}, C_m := \{(i - 1/2) \cdot h \mid i = 1, \ldots, n\}$, and $C_{\bar{m}} := \{(i - 1/2) \cdot h \mid i = 0, \ldots, m+1\}$. Define the function spaces

$$\mathcal{C}_{m\times n} = \{\phi : C_m \times C_n \to \mathbf{R}\}, \quad \mathcal{C}_{\bar{m}\times\bar{n}} = \{\phi : C_{\bar{m}} \times C_{\bar{n}} \to \mathbf{R}\}, \tag{11}$$

$$\mathcal{C}_{\bar{m}\times n} = \{\phi : C_{\bar{m}} \times C_n \to \mathbf{R}\}, \quad \mathcal{C}_{m\times\bar{n}} = \{\phi : C_m \times C_{\bar{n}} \to \mathbf{R}\}, \tag{12}$$

$$\mathcal{E}^{\mathrm{ew}}_{m\times n} = \{f : E_m \times C_n \to \mathbf{R}\}, \quad \mathcal{E}^{\mathrm{ns}}_{m\times n} = \{f : C_m \times E_n \to \mathbf{R}\}. \tag{13}$$

The functions of $\mathcal{C}_{m\times n}, \mathcal{C}_{\bar{m}\times n}, \mathcal{C}_{m\times\bar{n}}$, and $\mathcal{C}_{\bar{m}\times\bar{n}}$ are called *cell centered functions*, and we use the Greek symbols ϕ, ψ, and ζ to denote them. In component form cell-centered functions are identified via $\phi_{ij} := \phi(x_i, y_j)$, where $x_i = (i - 1/2) \cdot h, y_j = (j - 1/2) \cdot h$, and i and j can take on integer and half-integer values.

The functions of $\mathcal{E}^{\mathrm{ew}}_{m\times n}$ and $\mathcal{E}^{\mathrm{ns}}_{m\times n}$ are called *east–west edge-centered functions* and *north–south edge-centered functions*, respectively. We reserve the symbols f and g to denote these functions. In component form east–west edge-centered functions are identified via $f_{i+1/2,j} := f(x_{i+1/2}, y_j)$; north–south edge-centered functions are identified via $f_{ij+1/2} := f(x_i, y_{j+1/2})$.

We define the following weighted inner-products

$$(\phi\|\psi) = \sum_{i=1}^{m}\sum_{j=1}^{n}\phi_{i,j}\psi_{i,j}, \quad \phi,\psi \in \mathcal{C}_{m\times n}\cup\mathcal{C}_{\bar{m}\times n}\cup\mathcal{C}_{m\times\bar{n}}\cup\mathcal{C}_{\bar{m}\times\bar{n}}, \tag{14}$$

$$[f\|g]_{\mathrm{ew}} = \frac{1}{2}\sum_{i=1}^{m}\sum_{j=1}^{n}(f_{i+1/2,j}g_{i+1/2,j} + f_{i-1/2,j}g_{i-1/2,j}), \quad f,g \in \mathcal{E}^{\mathrm{ew}}_{m\times n}, \tag{15}$$

$$[f\|g]_{\mathrm{ns}} = \frac{1}{2}\sum_{i=1}^{m}\sum_{j=1}^{n}(f_{i,j+1/2}g_{i,j+1/2} + f_{i,j-1/2}g_{i,j-1/2}), \quad f,g \in \mathcal{E}^{\mathrm{ns}}_{m\times n}. \tag{16}$$

We will also need the following one-dimensional inner-products:

$$(f_{\star,j+1/2}|g_{\star,j+1/2}) = \sum_{i=1}^{m} f_{i,j+1/2}g_{i,j+1/2}, \quad (f_{i+1/2,\star}|g_{i+1/2,\star}) = \sum_{j=1}^{n} f_{i+1/2,j}g_{i+1/2,j}, \tag{17}$$

where the first is defined for $f, g \in \mathcal{E}^{\mathrm{ns}}_{m\times n}$, and the second for $f, g \in \mathcal{E}^{\mathrm{ew}}_{m\times n}$.

We define the edge-to-center difference operators $d_x : \mathcal{E}^{\mathrm{ew}}_{m\times n} \to \mathcal{C}_{m\times n}$ and $d_y : \mathcal{E}^{\mathrm{ns}}_{m\times n} \to \mathcal{C}_{m\times n}$ component-wise via

$$d_x f_{i,j} = \frac{1}{h}(f_{i+1/2,j} - f_{i-1/2,j}), \quad d_y f_{i,j} = \frac{1}{h}(f_{i,j+1/2} - f_{i,j-1/2}), \quad \begin{matrix} i = 1,\ldots,m, \\ j = 1,\ldots,n. \end{matrix} \tag{18}$$

The x-dimension center-to-edge average and difference operators, respectively, $A_x, D_x : \mathcal{C}_{\bar{m}\times n} \to \mathcal{E}^{\mathrm{ew}}_{m\times n}$ are defined component-wise as

$$A_x\phi_{i+1/2,j} = \frac{1}{2}(\phi_{i,j} + \phi_{i+1,j}), \quad D_x\phi_{i+1/2,j} = \frac{1}{h}(\phi_{i+1,j} - \phi_{i,j}), \quad \begin{matrix} i = 0,\ldots,m, \\ j = 1,\ldots,n. \end{matrix} \tag{19}$$

Likewise, the y-dimension center-to-edge average and difference operators, respectively, $A_y, D_y : \mathcal{C}_{m\times\bar{n}} \to \mathcal{E}^{\mathrm{ns}}_{m\times n}$ are defined component-wise as

$$A_y\phi_{i,j+1/2} = \frac{1}{2}(\phi_{i,j} + \phi_{i,j+1}), \quad D_y\phi_{i,j+1/2} = \frac{1}{h}(\phi_{i,j+1} - \phi_{i,j}), \quad \begin{matrix} i = 1,\ldots,m, \\ j = 0,\ldots,n. \end{matrix} \tag{20}$$

The standard 2D discrete Laplacian, $\Delta_h : \mathcal{C}_{\bar{m}\times\bar{n}} \to \mathcal{C}_{m\times n}$, is defined as

$$\Delta_h\psi_{i,j} = d_x(D_x\psi)_{i,j} + d_y(D_y\psi)_{i,j} = \frac{1}{h^2}(\psi_{i+1,j} + \psi_{i-1,j} + \psi_{i,j+1} + \psi_{i,j-1} - 4\psi_{i,j}), \quad \begin{matrix} i = 1,\ldots,m, \\ j = 1,\ldots,n. \end{matrix} \tag{21}$$

From these definitions, we obtain the following results [19]:

Proposition 1 (*Summation-by-parts*). *If $\phi \in \mathcal{C}_{\bar{m}\times n}\cup\mathcal{C}_{\bar{m}\times\bar{n}}$ and $f \in \mathcal{E}^{\mathrm{ew}}_{m\times n}$ then*

$$h^2[D_x\phi\|f]_{\mathrm{ew}} = -h^2(\phi\|d_x f) - h(A_x\phi_{1/2,\star}|f_{1/2,\star}) + h(A_x\phi_{m+1/2,\star}|f_{m+1/2,\star}), \tag{22}$$

and if $\phi \in \mathcal{C}_{m\times\bar{n}}\cup\mathcal{C}_{\bar{m}\times\bar{n}}$ and $f \in \mathcal{E}^{\mathrm{ns}}_{m\times n}$ then

$$h^2[D_y\phi\|f]_{\mathrm{ns}} = -h^2(\phi\|d_y f) - h(A_y\phi_{\star,1/2}|f_{\star,1/2}) + h(A_y\phi_{\star,n+1/2}|f_{\star,n+1/2}). \tag{23}$$

Proposition 2 (*Discrete Green's first identity*). Let $\phi,\psi \in \mathcal{C}_{\bar{m}\times\bar{n}}$. Then

$$\begin{aligned} h^2[D_x\phi\|D_x\psi]_{\mathrm{ew}} + h^2[D_y\phi\|D_y\psi]_{\mathrm{ns}} = {} & -h^2(\phi\|\Delta_h\psi) - h(A_x\phi_{1/2,\star}|D_x\psi_{1/2,\star}) + h(A_x\phi_{m+1/2,\star}|D_x\psi_{m+1/2,\star}) \\ & - h(A_y\phi_{\star,1/2}|D_y\psi_{\star,1/2}) + h(A_y\phi_{\star,n+1/2}|D_y\psi_{\star,n+1/2}). \end{aligned} \tag{24}$$

Proposition 3 (*Discrete Green's second identity*). *Let $\phi,\psi \in \mathcal{C}_{\bar{m}\times\bar{n}}$. Then*

$$\begin{aligned} h^2(\phi\|\Delta_h\psi) = {} & h^2(\Delta_h\phi\|\psi) + h(A_x\phi_{m+1/2,\star}|D_x\psi_{m+1/2,\star}) - h(D_x\phi_{m+1/2,\star}|A_x\psi_{m+1/2,\star}) - h(A_x\phi_{1/2,\star}|D_x\psi_{1/2,\star}) \\ & + h(D_x\phi_{1/2,\star}|A_x\psi_{1/2,\star}) + h(A_y\phi_{\star,n+1/2}|D_y\psi_{\star,n+1/2}) - h(D_y\phi_{\star,n+1/2}|A_y\psi_{\star,n+1/2}) - h(A_y\phi_{\star,1/2}|D_y\psi_{\star,1/2}) \\ & + h(D_y\phi_{\star,1/2}|A_y\psi_{\star,1/2}). \end{aligned} \tag{25}$$

We remark that these formulae have straightforward extensions to three dimensions.

3.2. Periodic boundary conditions

In this paper we are interested in periodic grid functions. Specifically, we shall say the cell-centered function $\phi \in \mathcal{C}_{\bar{m}\times\bar{n}}$ is periodic if and only if

$$\phi_{m+1,j} = \phi_{1,j}, \quad \phi_{0,j} = \phi_{m,j}, \quad j = 1, \ldots, n, \tag{26}$$
$$\phi_{i,n+1} = \phi_{i,1}, \quad \phi_{i,0} = \phi_{i,n}, \quad i = 0, \ldots, m+1. \tag{27}$$

For such functions, the center-to-edge averages and differences are periodic. For example, if $\phi \in \mathcal{C}_{\bar{m}\times\bar{n}}$ is periodic, then $A_x\phi_{m+1/2,j} = A_x\phi_{1/2,j}$ and also $D_x\phi_{m+1/2,j} = D_x\phi_{1/2,j}$, for all $j = 0, 1, \ldots, n+1$. We note that the results for periodic functions that are to follow also hold, in a possibly slightly modified form, when the boundary conditions are taken to be homogeneous Neumann,

$$\phi_{m+1,j} = \phi_{m,j}, \quad \phi_{0,j} = \phi_{1,j}, \quad j = 1, \ldots, n, \tag{28}$$
$$\phi_{i,n+1} = \phi_{i,n}, \quad \phi_{i,0} = \phi_{i,1}, \quad i = 0, \ldots, m+1, \tag{29}$$

or mixed periodic-homogeneous Neumann.

3.3. Norms

We use the following norms for cell-centered functions. If $\phi \in \mathcal{C}_{m\times n}$, then $\|\phi\|_2 := \sqrt{h^2(\phi\|\phi)}, \|\phi\|_4 := \sqrt{h^2(\phi^4\|\mathbf{1})}, \|\phi\|_\infty := \max_{\substack{1\leqslant i\leqslant m\\ 1\leqslant j\leqslant n}}|\phi_{i,j}|$, and we define $\|\nabla_h\phi\|_2$, where $\phi \in \mathcal{C}_{\bar{m}\times\bar{n}}$, to mean

$$\|\nabla_h\phi\|_2 := \sqrt{h^2[D_x\phi\|D_x\phi]_{\mathrm{ew}} + h^2[D_y\phi\|D_y\phi]_{\mathrm{ns}}}. \tag{30}$$

We will use the following discrete Sobolev-type norms for grid functions $\phi \in \mathcal{C}_{\bar{m}\times\bar{n}}$: $\|\phi\|_{0,2} := \|\phi\|_2$ and

$$\|\phi\|_{1,2} := \sqrt{\|\phi\|_2^2 + \|\nabla_h\phi\|_2^2}, \quad \|\phi\|_{2,2} := \sqrt{\|\phi\|^2 + \|\nabla_h\phi\|_2^2 + \|\Delta_h\phi\|_2^2}. \tag{31}$$

4. The numerical methods in detail and their properties

4.1. A convex splitting of the discrete energy

We begin by defining a fully discrete energy that is consistent with the continuous space energy (1). In particular, define the discrete energy $F : \mathcal{C}_{\bar{m}\times\bar{n}} \to \mathbf{R}$ to be

$$F(\phi) := \frac{1}{4}\|\phi\|_4 + \frac{1-\epsilon}{2}\|\phi\|_2^2 - \|\nabla_h\phi\|_2^2 + \frac{1}{2}\|\Delta_h\phi\|_2^2. \tag{32}$$

The following was proved in [19].

Proposition 4. *Suppose that $\phi \in \mathcal{C}_{\bar{m}\times\bar{n}}$ is periodic and that $\Delta_h\phi \in \mathcal{C}_{\bar{m}\times\bar{n}}$ is also periodic. Define the energies*

$$F_c(\phi) := \frac{1}{4}\|\phi\|_4^4 + \frac{1-\epsilon}{2}\|\phi\|_2^2 + \frac{1}{2}\|\Delta_h\phi\|_2^2, \quad F_e(\phi) := \|\nabla_h\phi\|_2^2. \tag{33}$$

Then the gradients of the respective energies are $\delta_\phi F_c = \phi^3 + (1-\epsilon)\phi + \Delta_h^2\phi$ and $\delta_\phi F_e = -2\Delta_h\phi$, and F_c and F_e are convex, provided $\epsilon < 1$. Hence F, as defined in (32), admits the convex splitting $F = F_c - F_e$.

The convex-splitting scheme for the PFC equation, proposed and analyzed in [19], is based on Proposition 4. In particular the scheme is the following: given $\phi^k \in \mathcal{C}_{\bar{m}\times\bar{n}}$ periodic, find $\phi^{k+1}, \mu^{k+1}, \kappa^{k+1} \in \mathcal{C}_{\bar{m}\times\bar{n}}$ periodic such that

$$\phi^{k+1} - \phi^k = s\{d_x(M(A_x\phi^k)D_x\mu^{k+1}) + d_y(M(A_y\phi^k)D_y\mu^{k+1})\}, \tag{34}$$

where $s > 0$ and

$$\mu^{k+1} := \delta_\phi F_c(\phi^{k+1}) - \delta_\phi F_e(\phi^k) = (\phi^{k+1})^3 + (1-\epsilon)\phi^{k+1} + 2\Delta_h\phi^k + \Delta_h\kappa^{k+1}, \tag{35}$$
$$\kappa^{k+1} := \Delta_h\phi^{k+1}. \tag{36}$$

The second-order scheme, though not specifically based on the convex splitting in Proposition 4, is similar to the scheme given above: given $\phi^k, \phi^{k-1} \in \mathcal{C}_{\bar{m}\times\bar{n}}$ periodic, find $\phi^{k+1}, \mu^{k+1/2}, \kappa^{k+1/2} \in \mathcal{C}_{\bar{m}\times\bar{n}}$ periodic such that

$$\phi^{k+1} - \phi^k = s\left\{d_x\left(M\left(\frac{3}{2}A_x\phi^k - \frac{1}{2}A_x\phi^{k-1}\right)D_x\mu^{k+1/2}\right) + d_y\left(M\left(\frac{3}{2}A_y\phi^k - \frac{1}{2}A_y\phi^{k-1}\right)D_y\mu^{k+1/2}\right)\right\}, \tag{37}$$

where $s > 0$ and

$$\mu^{k+1/2} := \frac{1}{4}(\phi^{k+1} + \phi^k)((\phi^{k+1})^2 + (\phi^k)^2) + \frac{1-\epsilon}{2}(\phi^{k+1} + \phi^k) + 3\Delta_h\phi^k - \Delta_h\phi^{k-1} + \Delta_h\kappa^{k+1/2}, \tag{38}$$
$$\kappa^{k+1/2} := \frac{1}{2}(\Delta_h\phi^{k+1} + \Delta_h\phi^k), \tag{39}$$

and $\phi^{-1} := \phi^0$.

4.2. Unconditional unique solvability of the schemes

We now show that both schemes are uniquely solvable for any time step.

Theorem 5. *The convex-splitting scheme (34) and the second-order* scheme (37) *are uniquely solvable for any time step-size* $s > 0$. *Moreover, both schemes are discretely mass conserving, i.e.,* $(\phi^{k+1} - \phi^k \| \mathbf{1}) = 0$.

Proof. This proof follows that of Thm. 3.4 in [19] and is based on a convexity argument. Discrete mass conservation follows from the following calulation: using summation-by-parts Proposition 1

$$(\phi^{k+1} - \phi^k \| \mathbf{1}) = s(d_x(M^\star_{\text{ew}} D_x \mu^\star) + d_y(M^\star_{\text{ns}} D_y \mu^\star) \| \mathbf{1}) = -s[M^\star_{\text{ew}} D_x \mu^\star \| D_x \mathbf{1}]_{\text{ew}} - s[M^\star_{\text{ns}} D_y \mu^\star \| D_y \mathbf{1}]_{\text{ns}} = 0, \tag{40}$$

where $M^\star_{\text{ew}}, M^\star_{\text{ns}}$, and $\mu^\star$ are the appropriate variables from the scheme (34) or the scheme (37). Thus, if the schemes have a solution ϕ^{k+1}, then by necessity it must be that $(\phi^{k+1} \| \mathbf{1}) = (\phi^k \| \mathbf{1})$, *i.e.*, ϕ^{k+1} and ϕ^k have equal means.

Now, without loss of generality, by rescaling the problem if necessary, we may suppose that $\phi^k \in H$, where H is the subspace of mean-zero functions in $\mathcal{C}_{m\times n}$. (If $\phi \in H$ then $(\phi \| \mathbf{1}) = 0$.) The appropriate space for solutions of both (34) and (37) must necessarily be H.

Suppose that $\phi \in \mathcal{C}_{\bar{m}\times\bar{n}}$ is periodic, such that $\Delta_h \phi \in \mathcal{C}_{\bar{m}\times\bar{n}}$ is also periodic. For the convex-splitting scheme (34) consider the following functional on H:

$$G_1(\phi) := \frac{h^2}{2}(\phi \| \phi)_{H,L_1} - h^2(\phi \| \phi^k)_{H,L_1} + F_c(\phi) - h^2(\phi \| \delta_\phi F_e(\phi^k)), \tag{41}$$

where the H, L_1 inner-product is defined as

$$(\phi_1 \| \phi_2)_{H,L_1} := [sM(A_x\phi^k) D_x\psi_1 \| D_x\psi_2]_{\text{ew}} + [sM(A_y\phi^k) D_y\psi_1 \| D_y\psi_2]_{\text{ns}} \tag{42}$$

and $\psi_i \in \mathcal{C}_{\bar{m}\times\bar{n}}$ is the unique solution [19, Lemma 3.2] to

$$L_1(\psi_i) := -sd_x(M(A_x\phi^k) D_x\psi_i) - sd_y(M(A_y\phi^k) D_y\psi_i) = \phi_i, \tag{43}$$

such that ψ_i is periodic and has mean zero $(\psi_i \| \mathbf{1}) = 0$. It is possible to show that (41) is *strictly* convex, and minimizing the strictly convex functional (41) is equivalent to solving (34). The complete details may be found in [19, Theorem 3.4].

For the second-order scheme (37) consider the alternate functional on H:

$$G_2(\phi) = \frac{h^2}{2}(\phi \| \phi)_{H,L_2} - h^2(\phi \| \phi^k)_{H,L_2} + Q(\phi) + h^2\left(\phi \middle\| \frac{1-\epsilon}{2}\phi^k + 3\Delta_h\phi^k - \Delta_h\phi^{k-1} + \frac{1}{2}\Delta_h^2\phi^k\right), \tag{44}$$

where

$$Q(\phi) = \frac{h^2}{4}\left(\frac{\phi^4}{4} + \frac{\phi^3}{3}\phi^k + \frac{\phi^2}{2}(\phi^k)^2 + \phi(\phi^k)^3 \| \mathbf{1}\right) + \frac{1-\epsilon}{4}\|\phi\|_2^2 + \frac{1}{4}\|\Delta_h\phi\|_2^2 \tag{45}$$

and where the H, L_2 inner-product is defined as

$$(\phi_1 \| \phi_2)_{H,L_2} := \left[sM\left(\frac{3}{2}A_x\phi^k - \frac{1}{2}A_x\phi^{k-1}\right) D_x\psi_1 \| D_x\psi_2\right]_{\text{ew}} + \left[sM\left(\frac{3}{2}A_y\phi^k - \frac{1}{2}A_y\phi^{k-1}\right) D_y\psi_1 \| D_y\psi_2\right]_{\text{ns}} \tag{46}$$

and $\psi_i \in \mathcal{C}_{\bar{m}\times\bar{n}}$ is the unique solution [19, Lemma 3.2] to

$$L_2(\psi_i) := -sd_x\left(M\left(\frac{3}{2}A_x\phi^k - \frac{1}{2}A_x\phi^{k-1}\right) D_x\psi_i\right) - sd_y\left(M\left(\frac{3}{2}A_y\phi^k - \frac{1}{2}A_y\phi^{k-1}\right) D_y\psi_i\right) = \phi_i, \tag{47}$$

such that ψ_i is periodic and has mean zero $(\psi_i \| \mathbf{1}) = 0$.

The functional Q is convex. This follows because $\|\phi\|_2^2$ and $\|\Delta_h\phi\|_2^2$ are convex (see [19]) and because

$$\frac{d^2}{d^2\phi}\left[\frac{1}{4}\left(\frac{\phi^4}{4} + \frac{\phi^3}{3}\phi^k + \frac{\phi^2}{2}(\phi^k)^2 + \phi(\phi^k)^3\right)\right] = \frac{1}{2}\phi^2 + \frac{1}{4}(\phi + \phi^k)^2 \geqslant 0. \tag{48}$$

Also note that by construction

$$\frac{d}{d\phi}\left[\frac{1}{4}\left(\frac{\phi^4}{4} + \frac{\phi^3}{3}\phi^k + \frac{\phi^2}{2}(\phi^k)^2 + \phi(\phi^k)^3\right)\right] = \frac{1}{4}(\phi + \phi^k)(\phi^2 + (\phi^k)^2), \tag{49}$$

where the right-hand-side is the nonlinear term in Eq. (38). Using the convexity of Q and the techniques in [19, Theorem 3.4], one may show that G_2 is *strictly* convex over H and that minimizing G_2 is equivalent to solving the second-order scheme (37), which completes the proof of the theorem. □

4.3. Unconditional stability of the schemes

The following result [19, Theorem 3.5] makes proving stability for the convex-splitting scheme (34) straightforward.

Proposition 6. *Suppose that $\phi^{k+1}, \phi^k \in \mathcal{C}_{\bar{m}\times\bar{n}}$ are periodic, and that $\Delta_h\phi^{k+1} \in \mathcal{C}_{\bar{m}\times\bar{n}}$ is also periodic. Assume that the discrete energy F admits the convex splitting $F = F_c - F_e$ above. Then*

$$F(\phi^{k+1}) - F(\phi^k) \leqslant h^2\,(\delta_\phi F_c(\phi^{k+1}) - \delta_\phi F_e(\phi^k)\|\phi^{k+1} - \phi^k). \tag{50}$$

The energy decay estimate in Propostion 6 readily yields the (strong) energy stability of the convex-splitting scheme.

Proposition 7. *Suppose that $\phi^k \in \mathcal{C}_{\bar{m}\times\bar{n}}$ is periodic and $\phi^{k+1} \in \mathcal{C}_{\bar{m}\times\bar{n}}$ is a solution to (34). The convex-splitting scheme (34) is unconditionally (strongly) energy stable, meaning that for any time step-size $s > 0$,*

$$F(\phi^{k+1}) \leqslant F(\phi^k). \tag{51}$$

Proof. Using the energy estimate and summation-by-parts Proposition 1, we have

$$\begin{aligned} F(\phi^{k+1}) - F(\phi^k) &\leqslant h^2(\delta_\phi F_c(\phi^{k+1}) - \delta_\phi F_e(\phi^k)\|\phi^{k+1} - \phi^k) = h^2(\mu^{k+1}\|s\{d_x(M(A_x\phi^k)D_x\mu^{k+1}) + d_y(M(A_y\phi^k)D_y\mu^{k+1})\}) \\ &= -sh^2\{[D_x\mu^{k+1}\|M(A_x\phi^k)D_x\mu^{k+1}]_{\mathrm{ew}} + [D_y\mu^{k+1}\|M(A_y\phi^k)D_y\mu^{k+1}]_{\mathrm{ns}}\} \leqslant 0. \qquad \square \end{aligned}$$

Remark 8. Note that the unconditional strong energy stability of (34) immediately implies the unconditional weak energy stability of the scheme. The latter means that for any time step-size $s > 0$ and any n

$$F(\phi^n) \leqslant F(\phi^0). \tag{52}$$

We cannot appeal to the energy decay estimate in Proposition 6 for the second-order scheme (37) because it does not specifically have the structure of a convex splitting. In fact, it appears that a statement of strong energy stability is not possible using the energy *F*. (We give a remark on this point after the next proposition.) However, weak energy stability suffices for our purposes.

Proposition 9. *Suppose that $\phi^k, \phi^{k-1} \in \mathcal{C}_{\bar{m}\times\bar{n}}$ are periodic, and that $\phi^{k+1} \in \mathcal{C}_{\bar{m}\times\bar{n}}$ is a solution to (37). The second-order scheme (37) is unconditionally (weakly) energy stable, meaning that for any time step-size $s > 0$ and any n*

$$F(\phi^n) \leqslant F(\phi^0). \tag{53}$$

Proof. We begin by defining

$$\|\nabla_h\mu^{k+1/2}\|_M^2 := h^2\left\{\left[D_x\mu^{k+1/2}\|M\left(\frac{3}{2}A_x\phi^k - \frac{1}{2}A_x\phi^{k-1}\right)D_x\mu^{k+1/2}\right]_{\mathrm{ew}} + \left[D_y\mu^{k+1/2}\|M\left(\frac{3}{2}A_y\phi^k - \frac{1}{2}A_y\phi^{k-1}\right)D_y\mu^{k+1/2}\right]_{\mathrm{ns}}\right\}. \tag{54}$$

Now suppose that $k \geqslant 1$. Taking the inner product of $\mu^{k+1/2}$ with (37) and using summation-by-parts Proposition 1 we obtain

$$-s\|\nabla_h\mu^{k+1/2}\|_M^2 = F(\phi^{k+1}) - F(\phi^k) + \|\nabla_h\phi^{k+1}\|_2^2 - \|\nabla_h\phi^k\|_2^2 + h^2(\phi^{k+1} - \phi^k\|3\Delta_h\phi^k - \Delta_h\phi^{k-1}). \tag{55}$$

With the identity

$$h^2(\phi^{k+1} - \phi^k\|3\Delta_h\phi^k - \Delta_h\phi^{k-1}) = -\|\nabla_h\phi^{k+1}\|_2^2 + \|\nabla_h\phi^k\|_2^2 + \|\nabla_h(\phi^{k+1} - \phi^k)\|_2^2 + h^2(\phi^{k+1} - \phi^k\|\Delta_h(\phi^k - \phi^{k-1})), \tag{56}$$

we have

$$F(\phi^{k+1}) - F(\phi^k) = -s\|\nabla_h\mu^{k+1/2}\|_M^2 - \|\nabla_h(\phi^{k+1} - \phi^k)\|_2^2 - h^2(\phi^{k+1} - \phi^k\|\Delta_h(\phi^k - \phi^{k-1})). \tag{57}$$

Using summation-by-parts and Cauchy's inequality, the last term satisfies

$$\begin{aligned} -h^2(\phi^{k+1} - \phi^k\|\Delta_h(\phi^k - \phi^{k-1})) &= h^2\{[D_x(\phi^{k+1} - \phi^k)\|D_x(\phi^k - \phi^{k-1})]_{\mathrm{ew}} + [D_y(\phi^{k+1} - \phi^k)\|D_y(\phi^k - \phi^{k-1})]_{\mathrm{ns}}\} \\ &\leqslant \frac{1}{2}\|\nabla_h(\phi^{k+1} - \phi^k)\|_2^2 + \frac{1}{2}\|\nabla_h(\phi^k - \phi^{k-1})\|_2^2. \end{aligned} \tag{58}$$

Combining (57) and (58) we have

$$F(\phi^{k+1}) - F(\phi^k) \leqslant -s\|\nabla_h\mu^{k+1/2}\|_M^2 - \frac{1}{2}\|\nabla_h(\phi^{k+1} - \phi^k)\|_2^2 + \frac{1}{2}\|\nabla_h(\phi^k - \phi^{k-1})\|_2^2. \tag{59}$$

For the $k = 0$ case, using that $\phi^0 = \phi^{-1}$, the last term on the right-hand-side of (57) disappears to yield

$$F(\phi^1) - F(\phi^0) = -s\|\nabla_h \mu^{1/2}\|_M^2 - \|\nabla_h(\phi^1 - \phi^0)\|_2^2. \tag{60}$$

Now, summing Eq. (59) we have

$$\begin{aligned} F(\phi^n) - F(\phi^1) &= \sum_{k=1}^{n-1}(F(\phi^{k+1}) - F(\phi^k)) \leqslant \sum_{k=1}^{n-1}\left(-s\|\nabla_h \mu^{k+1/2}\|_M^2 - \frac{1}{2}\|\nabla_h(\phi^{k+1} - \phi^k)\|_2^2 + \frac{1}{2}\|\nabla_h(\phi^k - \phi^{k-1})\|_2^2\right) \\ &= -s\sum_{k=1}^{n-1}\|\nabla_h \mu^{k+1/2}\|_M^2 - \frac{1}{2}\|\nabla_h(\phi^n - \phi^{n-1})\|_2^2 + \frac{1}{2}\|\nabla_h(\phi^1 - \phi^0)\|_2^2. \end{aligned} \tag{61}$$

Adding Eq. (60) to Eq. (61) yields

$$F(\phi^n) - F(\phi^0) \leqslant -s\sum_{k=0}^{n-1}\|\nabla_h \mu^{k+1/2}\|_M^2 - \frac{1}{2}\|\nabla_h(\phi^n - \phi^{n-1})\|_2^2 - \frac{1}{2}\|\nabla_h(\phi^1 - \phi^0)\|_2^2 \leqslant 0, \tag{62}$$

and the result is proven. □

Remark 10. An alternative approach to the question of energy stability is to introduce the discrete energy

$$\widetilde{F}(\phi^{k+1}, \phi^k) := F(\phi^{k+1}) + \frac{1}{2}\|\nabla_h(\phi^{k+1} - \phi^k)\|_2^2. \tag{63}$$

Inequality (59) shows that this energy is non-increasing from one time step to the next. In other words, the second-order scheme (37) is strongly energy stable with respect to $\widetilde{F}$. Moreover, $\widetilde{F}$ is consistent with E from (1) as h and s tend to zero.

Since both schemes are unconditionally weakly energy stable, using the methods in [19] we can show that both schemes are in fact stable in the infinity norm.

Theorem 11. *Let $\Phi(x,y)$ be a smooth, periodic function on $\Omega = (0, L_x) \times (0, L_y)$ and $\phi_{i,j}^0 := \Phi(x_i, y_j)$, and suppose E is the continuous energy (1). Let $\phi_{i,j}^k \in \mathcal{C}_{\bar{m}\times\bar{n}}$ be the k*th *periodic solution of either of the schemes (34) or (37). Then*

$$\|\phi^k\|_\infty \leqslant \sqrt{C_1 E(\Phi) + C_2 L_x L_y}, \tag{64}$$

where C_1 and C_2 are positive constants neither of which depend on on either s or h.

Remark 12. This last result holds also in one dimension. However, the proof presented in [19] does not automatically extend to three dimensions. This is because a discrete Sobolev inequality is used to translate energy stability into pointwise stability, and the inequality fails in three dimensions. We are currently studying the three dimensional case in further detail.

Using Theorem 11 and the techniques in [19], convergence of the schemes may be proven in one and two dimensions; in fact, this was done for the convex-splitting scheme (34) in [19].

5. Numerical solutions

In this section we discuss the practical numerical solution of both schemes (34) and (37) using the nonlinear multigrid method. Since the approach is quite similar for both schemes, we give the full details for the first (34), then point out what steps need to be modified for the second (37).

5.1. Nonlinear multigrid solution of the convex-splitting scheme

The scheme (34) is the following: find ϕ^{k+1}, μ^{k+1}, and κ^{k+1} in $\mathcal{C}_{\bar{m}\times\bar{n}}$ whose components solve

$$\phi_{i,j}^{k+1} - sd_x(M(A_x\phi^k)D_x\mu^{k+1})_{i,j} - sd_y(M(A_y\phi^k)D_y\mu^{k+1})_{i,j} = \phi_{i,j}^k, \tag{65}$$

$$\mu_{i,j}^{k+1} - (\phi_{i,j}^{k+1})^3 - (1-\epsilon)\phi_{i,j}^{k+1} - \Delta_h\kappa_{i,j}^{k+1} = 2\Delta_h\phi_{i,j}^k, \tag{66}$$

$$\kappa_{i,j}^{k+1} - \Delta_h\phi_{i,j}^{k+1} = 0, \tag{67}$$

where $\phi^{k+1}, \phi^k, \mu^{k+1}$, and κ^{k+1} are all assumed periodic. We use a nonlinear FAS multigrid method to solve the system (65)–(67) efficiently. This involves defining operator and source terms, which we do as follows. Let $\boldsymbol{\phi} = (\phi^{k+1}, \mu^{k+1}, \kappa^{k+1})^T$. Define the $3 \times m \times n$ nonlinear operator $\mathbf{N} = (N^{(1)}, N^{(2)}, N^{(3)})^T$ as

$$N_{i,j}^{(1)}(\boldsymbol{\phi}) = \phi_{i,j}^{k+1} - sd_x(M(A_x\phi^k)D_x\mu^{k+1})_{i,j} - sd_y(M(A_y\phi^k)D_y\mu^{k+1})_{i,j}, \tag{68}$$

$$N_{i,j}^{(2)}(\boldsymbol{\phi}) = \mu_{i,j}^{k+1} - (\phi_{i,j}^{k+1})^3 - (1-\epsilon)\phi_{i,j}^{k+1} - \Delta_h\kappa_{i,j}^{k+1}, \tag{69}$$

$$N_{i,j}^{(3)}(\boldsymbol{\phi}) = \kappa_{i,j}^{k+1} - \Delta_h\phi_{i,j}^{k+1} \tag{70}$$

and the $3 \times m \times n$ source $\mathbf{S} = (S^{(1)}, S^{(2)}, S^{(3)})^T$ as

$$S^{(1)}_{i,j}(\phi^k) = \phi^k_{i,j}, \quad S^{(2)}_{i,j}(\phi^k) = 2\Delta_h \phi^k_{i,j}, \quad S^{(3)}_{i,j}(\phi^k) = 0. \tag{71}$$

Then Eqs. (65)–(67) are equivalent to $\mathbf{N}(\boldsymbol{\phi}) = \mathbf{S}(\phi^k)$.

As we use a somewhat standard nonlinear FAS multigrid scheme (we refer the reader to Section 5.3 of Trottenberg et al. [15] for complete details), the only items to discuss in detail are the nonlinear smoothing scheme for the operator $\mathbf{N}$, and the interpolation operators for communicating between grids. For smoothing we use a nonlinear Gauss–Seidel method with Red–Black ordering. In what follows, to simplify the discussion, we give the details of the smoothing using the simpler Lexicographic ordering. Let ℓ be the index for the lexicographic Gauss–Seidel, and set $M^{\text{ew}}_{i+1/2,j} = M(A_x \phi^k_{i+1/2,j})$ and $M^{\text{ns}}_{ij+1/2} = M(A_y \phi^k_{ij+1/2})$. The smoothing scheme is as follows: for every (i,j), stepping lexicographically from (1,1) to (m,n), find $\phi^{k+1,\ell+1}_{ij}$, $\mu^{k+1,\ell+1}_{ij}$, and $\kappa^{k+1,\ell+1}_{ij}$ that solve

$$\begin{aligned}
&\phi^{k+1,\ell+1}_{ij} + \frac{s}{h^2}\left(M^{\text{ew}}_{i+1/2,j} + M^{\text{ew}}_{i-1/2,j} + M^{\text{ns}}_{ij+1/2} + M^{\text{ns}}_{ij-1/2}\right)\mu^{k+1,\ell+1}_{ij} \\
&\quad = S^{(1)}_{ij}(\phi^k) + \frac{s}{h^2}\left(M^{\text{ew}}_{i+1/2,j}\mu^{k+1,\ell}_{i+1j} + M^{\text{ew}}_{i-1/2,j}\mu^{k+1,\ell+1}_{i-1j} + M^{\text{ns}}_{ij+1/2}\mu^{k+1,\ell}_{ij+1} + M^{\text{ns}}_{ij-1/2}\mu^{k+1,\ell+1}_{ij-1}\right),
\end{aligned} \tag{72}$$

$$\begin{aligned}
&-\left(1 - \epsilon + 3\left(\phi^{k+1,\ell}_{ij}\right)^2\right)\phi^{k+1,\ell+1}_{ij} + \mu^{k+1,\ell+1}_{ij} + \frac{4}{h^2}\kappa^{k+1,\ell+1}_{ij} \\
&\quad = S^{(2)}_{ij}(\phi^k) - 2\left(\phi^{k+1,\ell}_{ij}\right)^3 + \frac{1}{h^2}\left(\kappa^{k+1,\ell}_{i+1j} + \kappa^{k+1,\ell+1}_{i-1j} + \kappa^{k+1,\ell}_{ij+1} + \kappa^{k+1,\ell+1}_{ij-1}\right),
\end{aligned} \tag{73}$$

$$\frac{4}{h^2}\phi^{k+1,\ell+1}_{ij} + \kappa^{k+1,\ell+1}_{ij} = S^{(3)}_{ij}(\phi^k) + \frac{1}{h^2}\left(\phi^{k+1,\ell}_{i+1j} + \phi^{k+1,\ell+1}_{i-1j} + \phi^{k+1,\ell}_{ij+1} + \phi^{k+1,\ell+1}_{ij-1}\right). \tag{74}$$

Note that we have used a local Newton linearization of the cubic term, but otherwise this is a standard vector application of Gauss–Seidel. This 3×3 linear system is unconditionally solvable, provided $\epsilon < 1$ (the determinant of the coefficient matrix is always positive in this case). We use Cramer's Rule to solve for $\phi^{k+1,\ell+1}_{ij}, \mu^{k+1,\ell+1}_{ij}$, and $\kappa^{k+1,\ell+1}_{ij}$.

Once a single, complete smoothing sweep is concluded, *i.e.*, all grid points have been traversed exactly once, we project the solution $(\phi^{k+1,\ell+1}_{ij}, \mu^{k+1,\ell+1}_{ij}, \kappa^{k+1,\ell+1}_{ij})$ to the space of periodic functions. In other words, we enforce the boundary conditions after a smoothing sweep. Three smoothing sweeps constitute the smoothing operation.

Finally, as we work on cell-centered grids, we use the interpolation operators most suited for this setting. In particular, for the restriction operator we use cell-center averaging, and for the prolongation operator we use piece-wise constant interpolation Section 2.8.4 [15].

5.2. Multigrid solution of the second-order scheme

Let $\boldsymbol{\phi} = (\phi^{k+1}, \mu^{k+1/2}, \kappa^{k+1/2})^T$. Define the $3 \times m \times n$ nonlinear operator $\mathbf{N}$ ass

$$N^{(1)}_{ij}(\boldsymbol{\phi}, \phi^k) = \phi^{k+1}_{ij} - sd_x\left(M\left(\frac{3}{2}A_x\phi^k - \frac{1}{2}A_x\phi^{k-1}\right)D_x\mu^{k+1/2}\right)_{ij} - sd_y\left(M\left(\frac{3}{2}A_y\phi^k - \frac{1}{2}A_y\phi^{k-1}\right)D_y\mu^{k+1/2}\right)_{ij}, \tag{75}$$

$$N^{(2)}_{ij}(\boldsymbol{\phi}, \phi^k) = \mu^{k+1/2}_{ij} - \frac{1}{4}(\phi^{k+1}_{ij} + \phi^k_{ij})((\phi^{k+1}_{ij})^2 + (\phi^k_{ij})^2) - \frac{1-\epsilon}{2}\phi^{k+1}_{ij} - \Delta_h\kappa^{k+1/2}_{ij}, \tag{76}$$

$$N^{(3)}_{ij}(\boldsymbol{\phi}, \phi^k) = \kappa^{k+1/2}_{ij} - \frac{1}{2}\Delta_h\phi^{k+1}_{ij} \tag{77}$$

and the $3 \times m \times n$ source $\mathbf{S} = (S^{(1)}, S^{(2)}, S^{(3)})^T$ as

$$S^{(1)}_{ij}(\phi^k, \phi^{k-1}) = \phi^k_{i,j}, \tag{78}$$

$$S^{(2)}_{ij}(\phi^k, \phi^{k-1}) = \frac{1-\epsilon}{2}\phi^k_{ij} + 3\Delta_h\phi^k_{ij} - \Delta_h\phi^{k-1}_{ij}, \tag{79}$$

$$S^{(3)}_{ij}(\phi^k, \phi^{k-1}) = \frac{1}{2}\Delta_h\phi^k_{ij}. \tag{80}$$

Again let ℓ be the index for the lexicographic Gauss–Seidel, and define

$$M^{\text{ew}}_{i+1/2,j} = M\left(\frac{3}{2}A_x\phi^k_{i+1/2,j} - \frac{1}{2}A_x\phi^{k-1}_{i+1/2,j}\right), \tag{81}$$

$$M^{\text{ns}}_{ij+1/2} = M\left(\frac{3}{2}A_y\phi^k_{ij+1/2} - \frac{1}{2}A_y\phi^{k-1}_{ij+1/2}\right). \tag{82}$$

The smoothing scheme is as follows: for every (i,j), stepping lexicographically from (1,1) to (m,n), find $\phi^{k+1,\ell+1}_{ij}$, $\mu^{k+1/2,\ell+1}_{ij}$, and $\kappa^{k+1/2,\ell+1}_{ij}$ that solve

$$\begin{aligned}
&\phi^{k+1,\ell+1}_{ij} + \frac{s}{h^2}\left(M^{\text{ew}}_{i+1/2,j} + M^{\text{ew}}_{i-1/2,j} + M^{\text{ns}}_{ij+1/2} + M^{\text{ns}}_{ij-1/2}\right)\mu^{k+1/2,\ell+1}_{ij} \\
&\quad = S^{(1)}_{ij}\left(\phi^k, \phi^{k-1}\right) + \frac{s}{h^2}\left(M^{\text{ew}}_{i+1/2,j}\mu^{k+1/2,\ell}_{i+1j} + M^{\text{ew}}_{i-1/2,j}\mu^{k+1/2,\ell+1}_{i-1j} + M^{\text{ns}}_{ij+1/2}\mu^{k+1/2,\ell}_{ij+1} + M^{\text{ns}}_{ij-1/2}\mu^{k+1/2,\ell+1}_{ij-1}\right),
\end{aligned} \tag{83}$$

$$-\left(\frac{1-\epsilon}{2}+\frac{1}{4}\left(\left(\phi_{i,j}^{k+1,\ell}\right)^2+\left(\phi_{i,j}^{k}\right)^2\right)\right)\phi_{i,j}^{k+1,\ell+1}+\mu_{i,j}^{k+1/2,\ell+1}+\frac{4}{h^2}\kappa_{i,j}^{k+1/2,\ell+1}$$
$$=S_{i,j}^{(2)}\left(\phi^k,\phi^{k-1}\right)+\frac{1}{4}\left(\left(\phi_{i,j}^{k+1,\ell}\right)^2+\left(\phi_{i,j}^{k}\right)^2\right)\phi_{i,j}^{k}+\frac{1}{h^2}\left(\kappa_{i+1,j}^{k+1/2,\ell}+\kappa_{i-1,j}^{k+1/2,\ell+1}+\kappa_{i,j+1}^{k+1/2,\ell}+\kappa_{i,j-1}^{k+1/2,\ell+1}\right), \tag{84}$$

$$\frac{2}{h^2}\phi_{i,j}^{k+1,\ell+1}+\kappa_{i,j}^{k+1/2,\ell+1}=S_{i,j}^{(3)}\left(\phi^k,\phi^{k-1}\right)+\frac{1}{2h^2}\left(\phi_{i+1,j}^{k+1,\ell}+\phi_{i-1,j}^{k+1,\ell+1}+\phi_{i,j+1}^{k+1,\ell}+\phi_{i,j-1}^{k+1,\ell+1}\right). \tag{85}$$

Here we have used a local Picard linearization of the cubic term in the Gauss–Seidel scheme. Again, a simple calculation of the determinate reveals that this 3×3 linear system is unconditionally solvable, provided $\epsilon<1$. We use Cramer's Rule to solve for $\phi_{i,j}^{k+1,\ell+1}$, $\mu_{i,j}^{k+1/2,\ell+1}$, and $\kappa_{i,j}^{k+1/2,\ell+1}$.

6. Numerical results

In this section we first demonstrate the convergence numerically of both the convex-splitting scheme (34) and the second-order scheme (37). We then present examples to show the power of the second-order method in computing the evolution of large systems.

6.1. Convergence of the convex-splitting scheme and the second-order scheme

To estimate the convergence rate with respect to a mesh with grid spacing h, simulations are performed using the three different grid spacings $2h, h$ and $h/2$. Since ϕ^h is defined at the cell centers, we define the Cauchy error between two different grid spacings ϕ^h and $\phi^{h/2}$ to be

$$e_{i,j}^{h:h/2}=\phi_{i,j}^{h}-\frac{1}{4}(\phi_{2i,2j}^{h/2}+\phi_{2i-1,2j}^{h/2}+\phi_{2i,2j-1}^{h/2}+\phi_{2i-1,2j-1}^{h/2}) \tag{86}$$

and correspondingly for $e^{2h:h}$. The rate of convergence is defined as

$$\log_2\left(\frac{\|e^{2h:h}\|_2}{\|e^{h:h/2}\|_2}\right). \tag{87}$$

We examine the convergence of our algorithm with the following initial data:

$$\phi(x,y)=0.07-0.02\cos\left(\frac{2\pi(x-12)}{32}\right)\sin\left(\frac{2\pi(y-1)}{32}\right)+0.02\cos^2\left(\frac{\pi(x+10)}{32}\right)\cos^2\left(\frac{\pi(y+3)}{32}\right)$$
$$-0.01\sin^2\left(\frac{4\pi x}{32}\right)\sin^2\left(\frac{4\pi(y-6)}{32}\right). \tag{88}$$

We point out that the numerical solutions evolve to a non-trivial state using this data. The domain is $\Omega=(0,32)\times(0,32)$ and the solution is evolved to time $t_{\text{final}}=10$, with $\epsilon=0.025$ and mobility $M(\phi)=1$. The grid sizes are $16^2, 32^2, 64^2, 128^2, 256^2$, and 512^2. The time step sizes are $s=0.025h^2$ for the convex-splitting scheme (34) and $s=0.05h$ for the second-order scheme (37). The stopping criterion for the nonlinear multigrid method is based on the magnitude of a scaled l_2 norm of the residual. In particular, if this is below a tolerance (1.0×10^{-12} here), the multigrid iteration is stopped. The errors and rates of convergence are shown in Tables 1 and 2. The results suggest that both schemes are second-order accurate in space, the convex-splitting scheme is first-order accurate in time and the second-order scheme is second-order accurate in time.

In Fig. 1, the time evolution of the scaled total energy $F/(L_xL_y)$ is shown for the convergence test, accompanied with the density field ϕ at the times $t=0$ and $t=10$. In Fig. 1(right), the white regions indicate $\phi=0.0685$; red, $\phi=0.097$; and blue, $\phi=0.04$. The second-order scheme (37) is used to generate plots, with $h=32/256$ and $s=0.05h$. The discrete energy is ob-

Table 1
Errors and convergence rates of the convex-splitting scheme (34). Parameters are given in the text, and the initial condition are defined in Eq. (88).

Grid sizes	16^2–32^2	32^2–64^2	64^2–128^2	128^2–256^2	256^2–512^2
Error	5.145×10^{-4}	2.457×10^{-4}	6.605×10^{-5}	1.669×10^{-5}	4.182×10^{-6}
Rate	1.066	1.895	1.985	1.997	

Table 2
Errors and convergence rates of the second-order scheme (37). Parameters are given in the text, and the initial condition are defined in Eq. (88).

Grid sizes	16^2–32^2	32^2–64^2	64^2–128^2	128^2–256^2	256^2–512^2
Error	5.535×10^{-4}	2.398×10^{-4}	6.202×10^{-5}	1.553×10^{-5}	3.882×10^{-6}
Rate	1.207	1.951	1.998	2.000	

served to be non-increasing from one time-step to the next, even though our theory only guarantees that the energy is bounded by its initial value (Proposition 9).

6.2. Analysis of effective time step

Following Cheng and Warren [2], we quantify how the numerical time step affects the dynamics during the evolution for both schemes. We simulate both schemes with the same random initial conditions on a square domain $(0,128)\times(0,128)$. In particular, $\phi^0_{i,j}=\bar{\phi}+\eta_{i,j}$, where $\bar{\phi}=0.07$ and $\eta_{i,j}$ is a random number satisfying $-\bar{\phi}\leqslant\eta_{i,j}\leqslant\bar{\phi}$. Further, $\epsilon=0.025$. For both schemes, simulations were performed with 4 different time steps: $s_1=0.01$ (first row, Figs. 2 and 3), $s_2=2$ (second row, Figs. 2 and 3), $s_3=10$ (third row, Figs. 2 and 3), and $s_4=20$ (fourth row, Figs. 2 and 3). The mesh size is $h=1.0$. In Figs. 2 and 3, the time evolution of the density field ϕ is shown, where white regions indicate $\phi=\bar{\phi}$; red, $\phi=\bar{\phi}+0.2$; and blue, $\phi=\bar{\phi}-0.2$. The first rows in Figs. 2 and 3 are obtained at the following numerical times: $t_1=450$, $t_2=900, t_3=1350$, and $t_4=2400$. Following Cheng and Warren, we compare results using different time steps *at the same discrete energy levels rather than at the same time*. That is, the energy associated with each column in Figs. 2 and 3 is equal. The associated times are listed in the figures.

From Fig. 2, we notice that the density fields obtained at the same energy levels using different time steps are qualitatively similar for the first-order scheme (34). However, the numerical times required to reach the same energy levels are dramatically different. For example, to reach the energy obtained at $t=2400$ using time step s_1, the scheme using time step s_3 requires simulation up to time $t=73640$, a factor of 30 increase! The second-order scheme (37) is more efficient however. A similar comparison using the second-order scheme reveals that the times required to reach the same energy level using different time steps are much better matched. Note that the result using the largest time step s_4 with the second-order scheme appears to be somewhat different from the others. This is explained below.

To make the comparison more quantitative, again following the analysis of Cheng and Warren [2], we use the solution with time step $s_1=0.01$ as a reference solution and use it to calculate scaled differences for the simulations using different time steps based column 1. More precisely, we define the scaled difference to be

$$D(s_i)=\frac{\|\phi(\cdot,t_1;s_1)-\phi(\cdot,t_1;s_i)\|_2}{\|\phi(\cdot,t_1;s_1)\|_2}, \tag{89}$$

where, recall, $t_1=450$. Fig. 4 shows $D(s_i)$ versus time step in a log-log plot where only the second-order scheme (37) is used. It indicates that the accuracy increases as the time step decreases and a scaled difference of 10% can be achieved with $s\approx 10$.

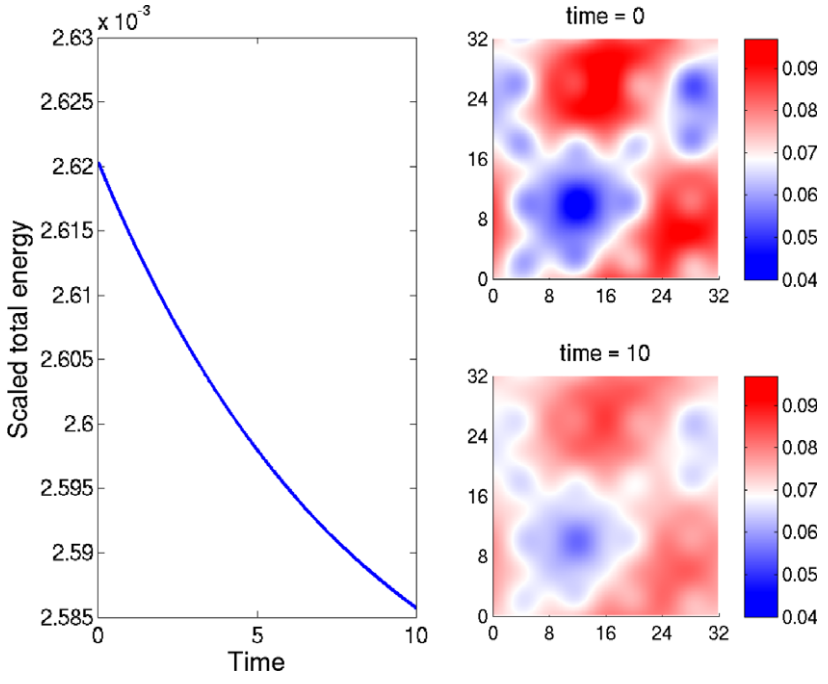

Fig. 1. The time evolution of the scaled total energy $F/(L_xL_y)$ is shown for the convergence test (left), accompanied with the density field ϕ at the times $t=0$ and $t=10$ (right). In the density plots, the white regions indicate $\phi=0.0685$; red, $\phi=0.097$; and blue, $\phi=0.04$. The initial condition is in Eq. (88), and the second-order scheme (37) is used to generate the plots, with $h=32/256=0.125$ and $s=0.05h$. Other parameters are given in the text.

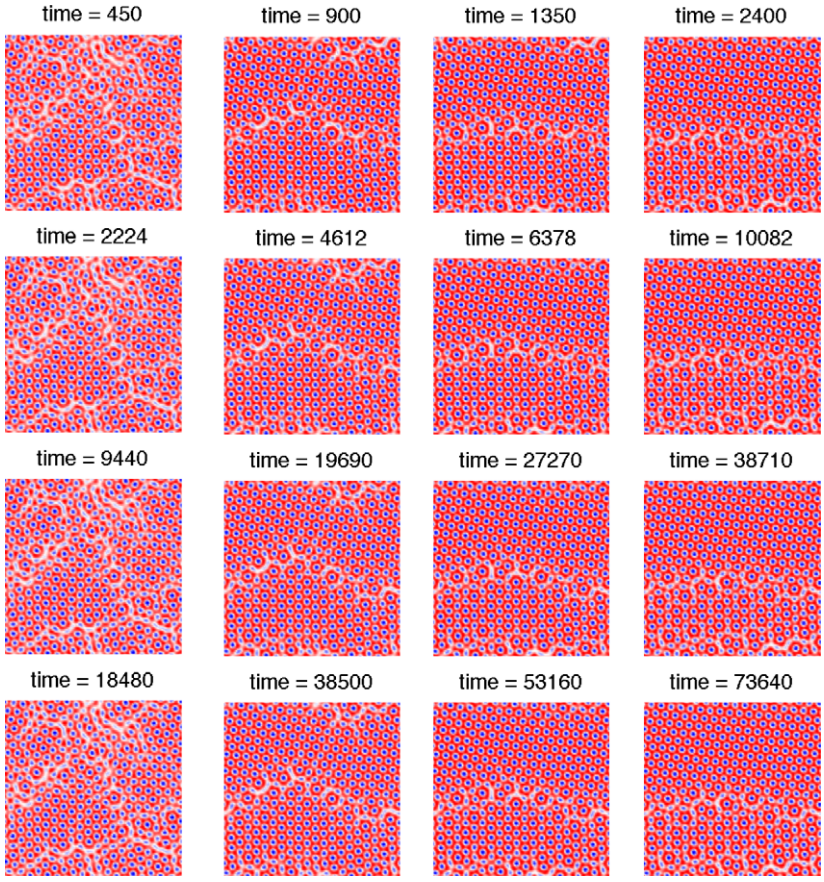

Fig. 2. The density fields ϕ computed with the convex-splitting scheme (34) using four different time steps: $s_1 = 0.01$ (row 1), $s_2 = 2.0$ (row 2), $s_1 = 10$ (row 3), and $s_1 = 20$ (row 4). The other parameters are given in the text. The results in each column correspond to the same discrete energy. The numerical time of each snapshot is shown on the top of the plot.

Also the scaled difference tends to saturate when the time step is large enough. This result is consistent with those obtained by Cheng and Warren using a much different scheme.

The evolution of scaled total energy obtained using the second-order scheme (37) with time step s_1 is shown in Fig. 5 (compare with the ϕ evolution in Fig. 3, row 1). Note that the scaled total energy decreases rapidly initially and is followed by slow evolution at later times.

To demonstrate how important it is to capture the fast early-time dynamics, we restart the second-order code with the solution obtained using the second-order scheme with $s_1 = 0.01$ at numerical time $t_1 = 450$ (row 1, column 1 of Fig. 3). Restarting the code from this time, with time steps s_2, s_3, and s_4, we observe significant improvement of the solution, especially, when the large time step $s_4 = 20$ is used. See results in Fig. 6. Recall from Fig. 3 that the density fields using time step s_4 are qualitatively different from those using the other three (smaller) time steps when all schemes are started from the $t = 0$ data.

As suggested by these results, the reason for the difference is that using the largest time step s_4 in the second-order scheme does not accurately capture the rapid, early-time dynamics. Observe that for all the cases in Fig. 6, the times required to evolve to the same energy levels are much better matched when the early-time dynamics are captured with a small time step. This suggests that performance of the scheme could be further enhanced by using an adaptive time step. This is currently under study.

6.3. Dynamics of polycrystals and grain boundaries

We now use the second-order scheme (37) to simulate the growth of a polycrystal and the dynamics of grain boundaries in a supercooled liquid. We simulate a system on a square domain: $(0, 804) \times (0, 804)$ with $\bar{\phi} = 0.285$ and $\epsilon = 0.25$, where $\bar{\phi}$ is the average of ϕ. The numerical parameters are $s = 1$ and $h = 0.4$ (2048 grid points in each direction). The initial configuration of ϕ consists of 3 groupings of random fluctuations located at the bottom of the domain, *i.e.*, $y = 0$, in an otherwise homogeneous environment. The random fluctuations have amplitude $\bar{\phi}$. Neumann boundary conditions are used for the ver-

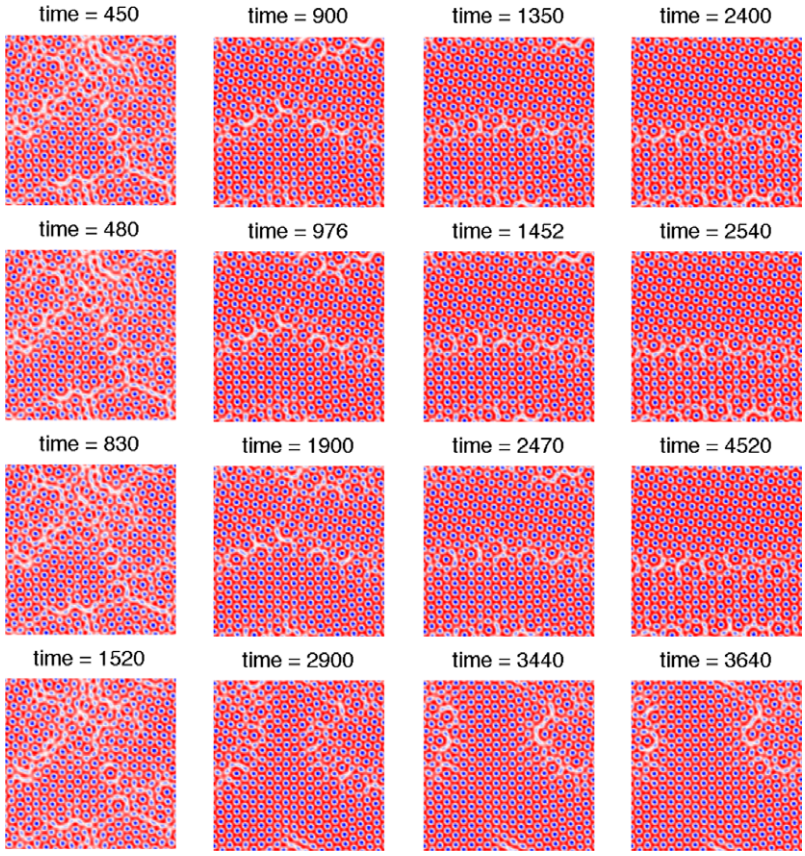

Fig. 3. The density fields ϕ computed with the second-order scheme (37) using four different time steps: $s_1 = 0.01$ (row 1), $s_2 = 2.0$ (row 2), $s_3 = 10$ (row 3), and $s_4 = 20$ (row 4). The other parameters are given in the text. The results in each column correspond to the same discrete energy. The numerical time of each snapshot is shown on the top of the plot.

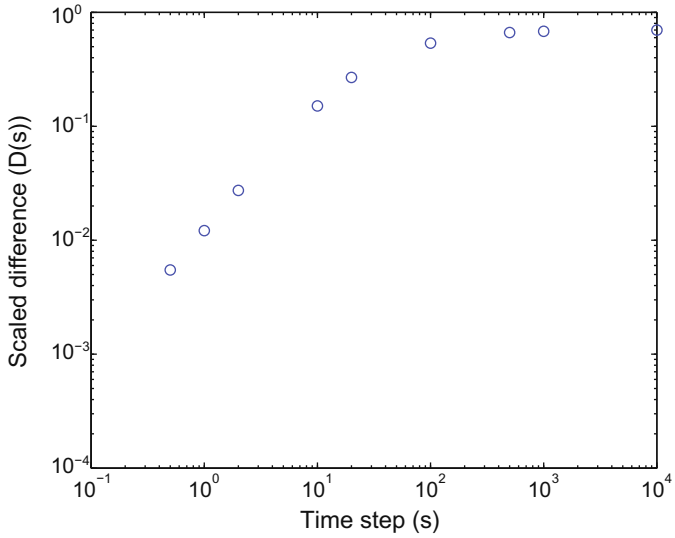

Fig. 4. The scaled difference, defined in Eq. (89) is plotted versus time step in a log–log plot. The second-order scheme (37) is used in the calculations. The parameters are given in the text and are the same as those used to produce Fig. 3.

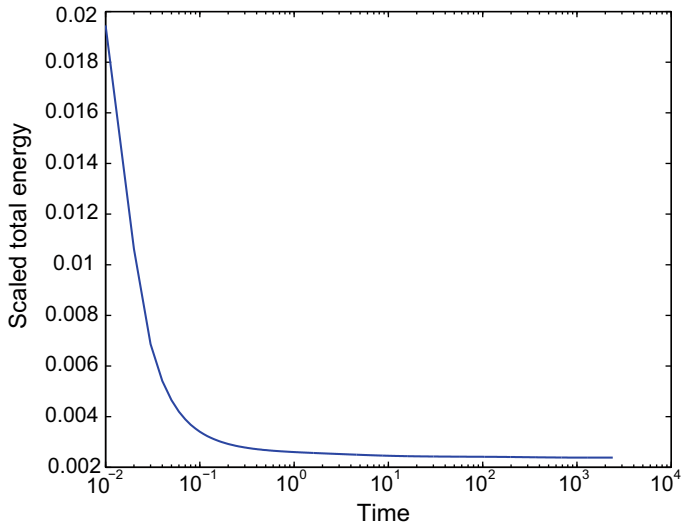

Fig. 5. The time evolution of the scaled total energy for the simulation represented in row 1 of Fig. 3. In particular, the second-order PFC scheme (37) with the time step size $s_1 = 0.01$ generated the result. The time axis is in log scale, whereas the energy axis is in linear scale. Note that the scaled total energy decreases rapidly initially and is followed by slow evolution at later times.

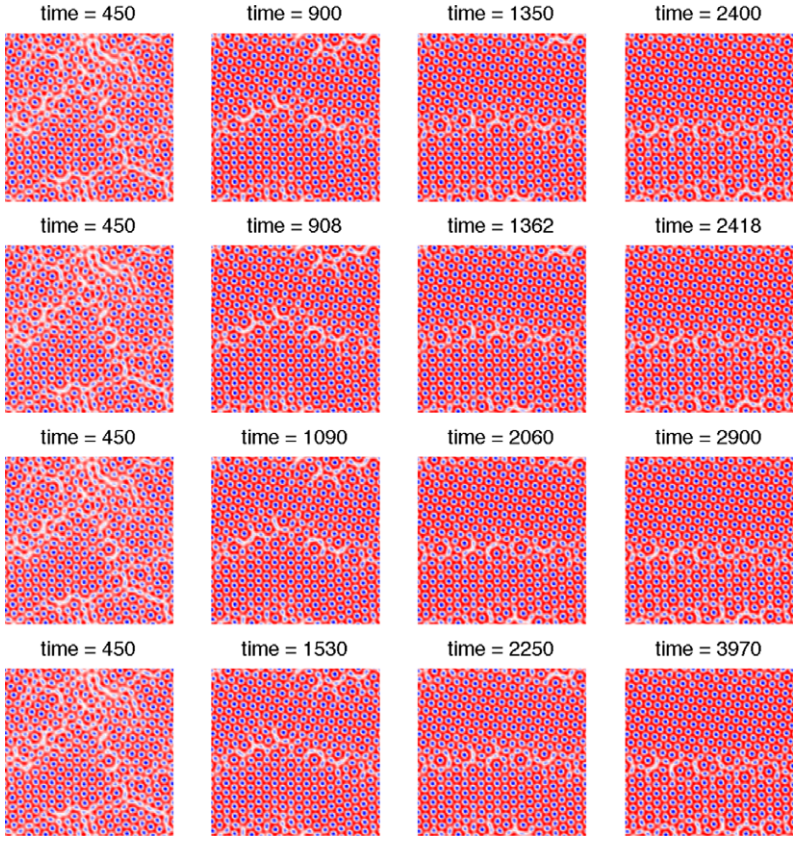

Fig. 6. The density fields ϕ computed with the second-order scheme (37) using four different time steps: $s_1 = 0.01$ (row 1), $s_2 = 2.0$ (row 2), $s_3 = 10$ (row 3), and $s_4 = 20$ (row 4). The calculations were initialized with the computed density field ϕ at numerical time $t_1 = 450$ using result from the simulation using the time step size $s_1 = 0.01$ from Fig. 3 (*i.e.*, row 1, column 1 of Fig. 3). The other parameters are given in the text and are the same as those used to generate Figs. 2 and 3. The results in each column correspond to the same discrete energy. The numerical time of each snapshot is shown on the top of the plot.

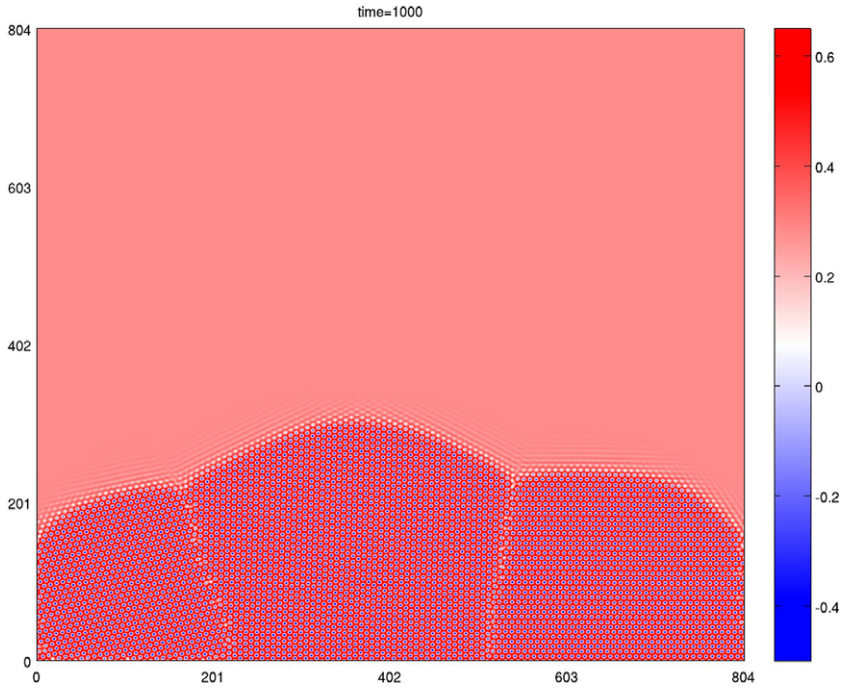

Fig. 7(a). Heterogeneous nucleation of three crystallites in a supercooled liquid. The snapshot shows the density field ϕ at time $t = 1000$. The parameters are $\bar{\phi} = 0.285, \epsilon = 0.25, s = 1$, and $h = 0.4$ (2048 grid points in each direction). The second-order scheme (37) is used in the calculation.

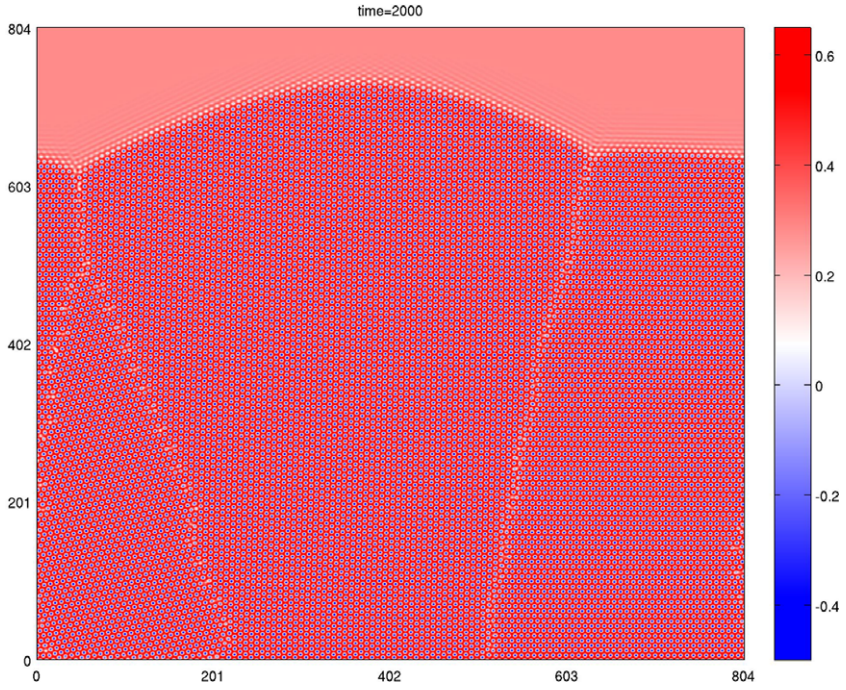

Fig. 7(b). Heterogeneous nucleation of three crystallites in a supercooled liquid. The snapshot shows the density field ϕ at time $t = 2000$. The parameters are $\bar{\phi} = 0.285, \epsilon = 0.25, s = 1$, and $h = 0.4$ (2048 grid points in each direction). The second-order scheme (37) is used in the calculation.

tical directions whereas periodic boundary conditions are used in the horizontal directions. As shown in Figs. 7(a), 7(b), 7(c), the initial configuration evolves into three crystallites, each with a different orientation and a well-defined liquid/crystal interface. As time evolves the crystallites impinge upon one another and form grain boundaries. We remark that this result

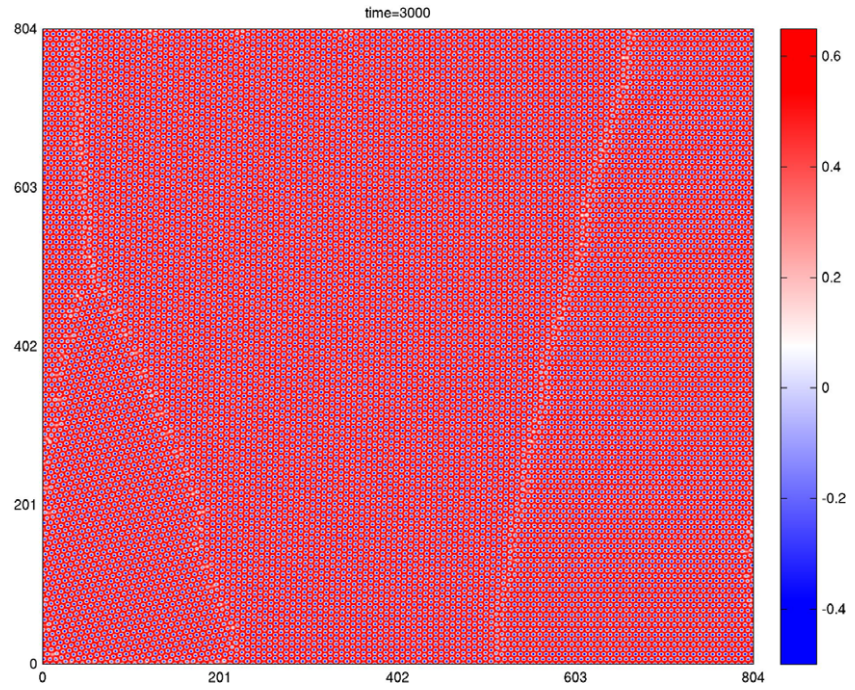

Fig. 7(c). Heterogeneous nucleation of three crystallites in a supercooled liquid. The snapshot shows the density field ϕ at time $t = 3000$. The parameters are $\bar{\phi} = 0.285, \epsilon = 0.25, s = 1$, and $h = 0.4$ (2048 grid points in each direction). The second-order scheme (37) is used in the calculation.

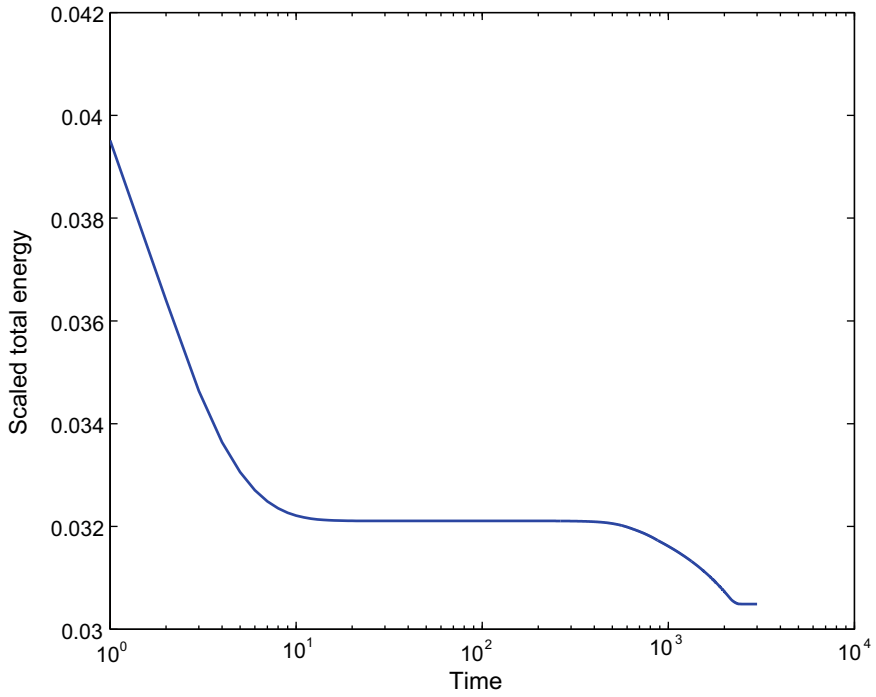

Fig. 7(d). The evolution of the scaled total energy during the heterogeneous nucleation and growth of three crystallites in a supercooled liquid shown in (a)–(c). The time axis is in log scale, whereas the energy axis is in linear scale. Note that the scaled total energy decreases rapidly initially and is followed by slow evolution at later times.

is qualitatively similar to one obtained by Elder et al. [4]. The evolution of the scaled total energy is shown in Fig. 7(d). This plot shows what is typically observed: even though strong energy stability has not been established for (37), one typically observes that the energy is non-increasing from one time step to the next. This simulation also provides further evidence

that adaptive time stepping could improve the efficiency of the schemes dramatically, since the late-time dynamics operates on a much slower time scale than the early-time dynamics.

7. Conclusions

In this paper, we have presented and compared two unconditionally energy stable finite-difference schemes for the sixth-order phase field crystal (PFC) equation. The first is a one-step scheme based on a convex splitting of a discrete energy and is first order in time and second order in space. The second is a two-step scheme and is fully second-order. In both cases the equations at the implicit time level are nonlinear but represent the gradients of strictly convex functions and are thus uniquely solvable, regardless of time step-size. The convergence of the schemes was demonstrated numerically. Our analysis of the effective time step suggests that the error saturates when the time step is sufficiently large, and is consistent with the results of study done by Cheng and Warren [2]. A comparison between the convex-splitting scheme (34) and the second-order scheme (37) reveals that the second-order scheme is more efficient and tends to give a very accurate solution, provided the fast time scale dynamics are accurately captured.

In the future, we plan to develop an adaptive time stepping algorithm together with the energy stable methods described here. We anticipate that this will be very effective in accelerating phase field crystal simulations since the dynamics typically involve a slowly evolving microstructure punctuated by a few rapid events. In forthcoming papers [7,17] we analyze and test numerically convex splitting schemes for the modified phase field crystal (MPFC) equation, which was proposed in [12] and takes into account elastic waves. Finally, we plan to use the new algorithms to investigate the epitaxial growth of nanoscale thin films.

Acknowledgments

The authors thank Axel Voigt, Ken Elder, and Mikko Haataja for valuable discussions. ZH, SMW and JSL gratefully acknowledge partial support from the National Science Foundation Division of Mathematical Sciences (DMS) and Division of Materials Research (DMR). Zhengzheng Hu was also partially supported by a Doctoral Dissertation Fellowship from the Graduate School at the University of California, Irvine.

References

[1] R. Backofen, A. Rätz, A. Voigt, Nucleation and growth by a phase field crystal (PFC) model, Phil. Mag. Lett. 87 (2007) 813.
[2] M. Cheng, J.A. Warren, An efficient algorithm for solving the phase field crystal model, J. Comput. Phys. 227 (2008) 6241.
[3] K.R. Elder, M. Grant, Modeling elastic and plastic deformations in nonequilibrium processing using phase filed crystal, Phys. Rev. E 90 (2002) 051605.
[4] K.R. Elder, M. Katakowski, M. Haataja, M. Grant, Modeling elasticity in crystal growth, Phys. Rev. Lett. 88 (2002) 245701.
[5] D. Eyre, Unconditionally gradient stable time marching the Cahn–Hilliard equation, in: J.W. Bullard, R. Kalia, M. Stoneham, L.Q. Chen (Eds.), Computational and Mathematical Models of Microstructural Evolution, vol. 53, Materials Research Society, Warrendale, PA, USA, 1998, pp. 1686–1712.
[6] Y. He, Y. Liu, T. Tang, On large time-stepping methods for the Cahn–Hilliard equation, Appl. Numer. Math. 57 (4) (2006) 616–628.
[7] Z. Hu, S. Wise, C. Wang, J.S. Lowengrub, Stable and efficient finite-difference nonlinear-multigrid schemes for the modified phase field crystal equation, in preparation.
[8] J.S. Kim, K. Kang, J.S. Lowengrub, Conservative multigrid methods for Cahn–Hilliard fluids, J. Comput. Phys. 193 (2003) 511–543.
[9] P.H. Leo, J.S. Lowengrub, H.J. Jou, A diffuse interface model for microstructural evolution in elastically stressed solids, Acta Mater. 46 (1997) 2113.
[10] U.M.B. Marconi, P. Tarazona, Dynamic density functional theory of liquids, J. Chem. Phys. 110 (1999) 8032.
[11] J. Mellenthin, A. Karma, M. Plapp, Phase-field crystal study of grain-boundary premelting, Phys. Rev. B 78 (2008) 184110.
[12] M. Haataja, P. Stefanovic, N. Provatas, Phase-field crystals with elastic interactions, Phys. Rev. Lett. 96 (2006) 225504.
[13] N. Provatas, J.A. Dantzig, B. Athreya, P. Chan, P. Stefanovic, N. Goldenfeld, K.R. Elder, Using the phase-field crystal method in the multiscale modeling of microstructure evolution, JOM 59 (2007) 83.
[14] J. Swift, P.C. Hohenberg, Hydrodynamic fluctuations at the convective instability, Phys. Rev. A 15 (1977) 319.
[15] U. Trottenberg, C.W. Oosterlee, A. Schüller, Multigrid, Academic Press, New York, 2005.
[16] B.P. Vollmayr-Lee, A.D. Rutenberg, Fast and accurate coarsening simulation with an unconditionally stable time step, Phys. Rev. E 68 (2003) 066703.
[17] C. Wang, S. Wise, An energy stable and convergent finite-difference scheme for the modified phase field crystal equation, SIAM J. Numer. Anal., submitted for publication.
[18] S.M. Wise, J.S. Kim, J.S. Lowengrub, Solving the regularized, strongly anisotropic Chan–Hilliard equation by an adaptive nonlinear multigrid method, J. Comput. Phys. 226 (2007) 414–446.
[19] S.M. Wise, C. Wang, J.S. Lowengrub, An energy stable and convergent finite-difference scheme for the phase field crystal equation, SIAM J. Numer. Anal., in press.
[20] C. Xu, T. Tang, Stability analysis of large time-stepping methods for epitaxial growth models, SIAM J. Numer. Anal. 44 (2006) 1759–1779.